

MEDPSeg: End-to-end segmentation of pulmonary structures and lesions in computed tomography

Diedre S. Carmo, Jean Ribeiro, Alejandro P. Comellas, Joseph M. Reinhardt *Fellow, IEEE*, Sarah E. Gerard, Leticia Rittner *Senior Member, IEEE*, Roberto A. Lotufo

Abstract—The COVID-19 pandemic response highlighted the potential of deep learning methods in facilitating the diagnosis and prognosis of lung diseases through automated segmentation of normal and abnormal tissue in computed tomography (CT). Such methods not only have the potential to aid in clinical decision-making but also contribute to the comprehension of novel diseases. In light of the labor-intensive nature of manual segmentation for large chest CT cohorts, there is a pressing need for reliable automated approaches that enable efficient analysis of chest CT anatomy in vast research databases, especially in more scarcely annotated targets such as pneumonia consolidations. A limiting factor for the development of such methods is that most current models optimize a fixed annotation format per network output. To tackle this problem, polymorphic training is used to optimize a network with a fixed number of output channels to represent multiple hierarchical anatomic structures, indirectly optimizing more complex labels with simpler annotations. We combined over 6000 volumetric CT scans containing varying formats of manual and automated labels from different sources, and used polymorphic training along with multitask learning to develop MEDPSeg, an end-to-end method for the segmentation of lungs, airways, pulmonary artery, and lung lesions with separation of ground glass opacities, and parenchymal consolidations, all in a single forward prediction. We achieve state-of-the-art performance in multiple targets, particularly in the segmentation of ground glass opacities and consolidations, a challenging problem with limited manual annotation availability. In addition, we provide an open-source implementation with a graphical user interface at <https://github.com/MICLab-Unicamp/medpseg>.

Index Terms—deep learning, pulmonary segmentation, lung lesions, polymorphic training, computed tomography

D. Carmo is supported by São Paulo Research Foundation (FAPESP) grants #2019/21964-4 and #2022/02344-8. R. Lotufo and L. Rittner are partially supported by CNPq (The Brazilian National Council for Scientific and Technological Development) under grants 313047/2022-7 and 313598/2020-7, and Coordenação de Aperfeiçoamento de Pessoal de Nível Superior (CAPES) under grant 506728/2020-00.

D. S. Carmo, J. Ribeiro, L. Rittner and R. A. Lotufo are with the Department of Computer Engineering and Automation, School of Electrical and Computer Engineering, Universidade Estadual de Campinas, Campinas, SP, Brazil (e-mail: lrittner@unicamp.br).

A. P. Comellas is with the Department of Internal Medicine, University of Iowa, Iowa City, IA, United States (e-mail: alejandro-comellas@uiowa.edu).

J. M. Reinhardt and S. E. Gerard are with the Roy J. Carver Department of Biomedical Engineering, University of Iowa, Iowa City, IA, United States (e-mail: sarah-gerard@uiowa.edu).

I. INTRODUCTION

The COVID-19 pandemic showcased the possible contributions of automated deep learning segmentation methods to assist medical doctors in the quick diagnosis and prognostication of lung diseases using medical imaging [1]. These methods also contribute to the understanding of pathophysiological processes of novel diseases through medical research, such as correlating lung parenchyma lesions in computed tomography (CT) with Long COVID demographic information [2]. Moreover, morphological assessment of the airways has been correlated with lung disease severity [3]. Pulmonary artery measurements are used for pulmonary hypertension diagnosis and thoracic surgery guidance [4]. The development of automated and reliable segmentation of pulmonary structures in CT images is a critical step in enabling accurate quantitative CT and the discovery of image-based biomarkers.

Manual segmentation of pulmonary structures in CT is prohibitively time consuming and cost intensive. With increased access to CT scans resulting in the availability of large research databases [1], [3], [4], it is paramount for future decision-support systems and medical research to have access to general automated methods enabling fast and reliable analysis of normal and abnormal anatomy. Increased availability of training data, recent advancements in deep learning, and UNet-like convolutional neural networks (CNN) [5], [6] have accelerated performance improvement in the automated segmentation of chest CT structures over the last decade [7]. However, the generalization capabilities of deep learning methods are still relatively poor in tasks with a limited amount of high-quality manual annotation and thus low data variability, such as the separation of ground glass opacities (GGO) and parenchymal consolidations in the lung [8], [9]. This limits the adoption of deep learning-based methods in day-to-day medical research or even clinical use [10], [11]. In this work, we propose a way to circumvent this data variability limitation by exploiting hierarchical properties of lung annotations, silver standard labels, and multitask learning, achieving state-of-the-art performance in multiple chest CT targets, especially consolidation segmentation.

A. Related Work

Recent work has achieved stable and generalizable results in the case of some segmentation targets, such as the lung parenchyma, even in the presence of abnormalities. Hofmanninger et al. [12] suggest that the large amount of data variability used in their method, Lungmask, was the most important contribution for its impressive performance. nnUNet [6], an adaptable framework that automatically trains a UNet model to the provided imaging and label pairs, makes heavy use of data preprocessing, normalization and augmentation to achieve state-of-the-art performance in multiple medical imaging segmentation challenges, also raising the importance of the data processing pipeline step and data variance. Challenges that nnUNet was in the top performing submissions include the Airway Tree Modelling challenge (ATM 2022) [3], Pulmonary Artery Segmentation Challenge (PARSE 2022) [4] and the COVID-19 Lung CT Lesion Segmentation Challenge [13]. There have been many other proposals for automated segmentation of COVID-19 pneumonia-related lesions, including a past version of this work's architecture [14], where we adapted the object detection network, EfficientDet [15] for multitask learning for lung and lung lesions segmentation. Another example is CopleNet [16] which uses a noise-robust Dice [17] loss modification and an exponential moving average of a novel architecture as a teacher network that is only updated when the student has a low loss.

A limitation of deep learning-based medical image segmentation methods is the adherence to a specific label format from specific datasets, due to the inherent limitation of a fixed number of output channels in CNN architecture design. Usually, the involvement of multiple structures includes a single one-hot annotation for all structures in all training cases [18]. Alternatively, multitask learning allows different label formats by using multiple decoder branches with a different number of output channels [19], [20]. However, this approach is not suitable in applications with a scarce amount of manual annotations available for specific task, e.g., separating general lung lesions into specific GGO and consolidation regions. Medical literature commonly uses approximated separations through Hounsfield unit (HU) thresholds [21]. In addition, existing manual labels are noisy due to ambiguous boundaries [8], [22]. This hinders the segmentation performance of supervised models even when using heavy data augmentation. To solve this problem, semi-supervised approaches attempt to leverage information from unlabeled data. For example, InfNet [8] uses a random propagation strategy which generates pseudo labels for unlabeled data using a trained network, and iteratively trains new networks with these pseudo labels.

For the segmentation of pulmonary and circulatory targets in general, using information from neighboring anatomy has been shown to be effective. For example, unsupervised segmentation of the rib cage and airways can be used to constrain the lung parenchyma location and to guide lung lobe segmentation [7]. One can also use information from the hierarchical properties of the labeled structures. This approach has shown promising results both in natural [23] and medical [24] images, however, with annotations still confined to the same dataset. Gerard

et al. [25] coined the term polymorphic training for a new flexible training approach with different lung parenchyma label formats, sourced from different datasets and representing different species. In their work, the boundary between the left and right lung is not defined and not included in the label of an animal lung, however, polymorphic learning was used to incorporate left/right labels of the human lung from a different dataset, allowing for the separation of the animal lung in the trained network's prediction. This was achieved with the reduction of two left and right output channels through a sum operation in real-time during training, which indirectly optimizes the gradient of the separation even when the label is binary.

B. Contributions

Our main hypothesis is that: merging multitasking, polymorphic learning, and silver standard (automated) labels for increased variability in training would lead to an efficient method for multi-label chest CT assessment, and improved results in specific problems that do not have a lot of annotated ground truth. In this work, we expand the polymorphic training concept from Gerard et al. [25] to multiple levels of hierarchy, due to the anatomical relationship that GGO and consolidations are part of general lung lesion annotations, and lung lesions are part of general lung labels (Fig. 1). Consequently, we are able to mix labels of different formats from multiple datasets optimizing the same fixed network output, while showing the network a large variety of CT scans of multiple diseases. In addition, we show performance improvements from multitasking airway and pulmonary artery segmentation. Modified EfficientDet for Polymorphic Pulmonary Segmentation (MEDPSeg) is presented as a state-of-the-art end-to-end model for the automated segmentation of: lung; lung lesions; separation of lung lesions into GGOs and consolidations; airway; and pulmonary artery, in a single forward pass. More than 6000 volumetric CT scans from multiple sources are included in the training, with manual (gold standard) and automated (silver standard) labels from teacher networks. MEDPSeg is optimized in all target formats at the same time and has statistically equivalent or superior quantitative metrics when compared to state-of-the-art methods specialized in each involved target. Additionally, open-source implementation, trained weights, a python pip package, and an easy-to-use tool with a graphical user interface (GUI) are provided.

II. DATA

Multiple independent data sources were used in this study. Datasets with voxel-level annotation performed by human experts are referred to as "gold standard" datasets or gold data for short (Section II-A). Datasets annotated with automated methods are referred to as "silver standard" or silver data (Section II-B).

A. Gold data

Each CT image with manual voxel-level annotations contains one of the following targets: healthy and lesion areas; GGO and consolidation; airway; or pulmonary artery (Table I).

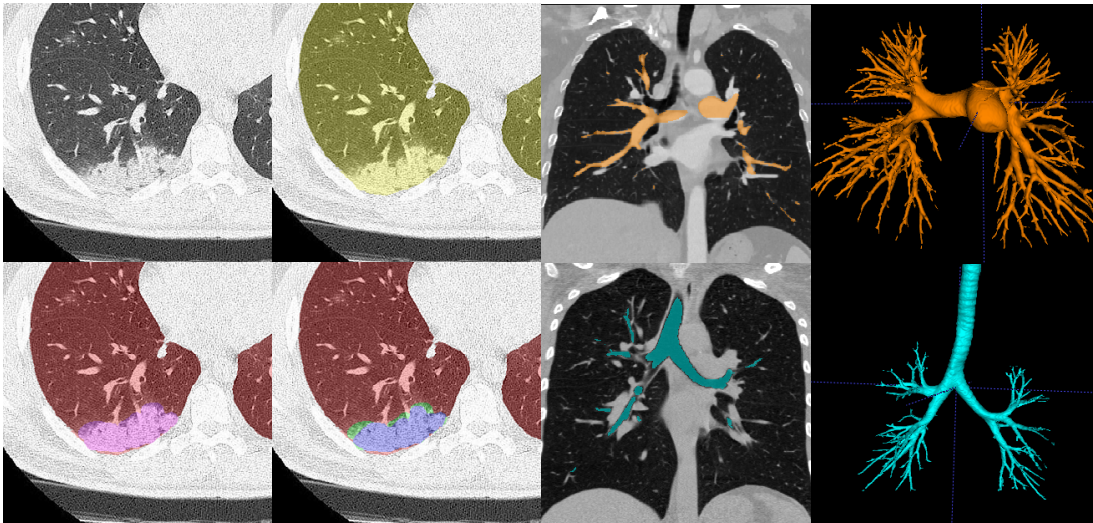


Fig. 1. Illustration of all target formats used in this work. Axial slices show the hierarchical properties of lung lesion annotation with whole lung in yellow, healthy tissue in red, lesions in magenta, GGO in green, and consolidations in blue. Circulatory annotations are overlaid on coronal CT slices, with airways in cyan and arterial tree in orange. Volumetric visualizations created with ITK-Snap [26].

Dataset Name	Label Format	N. images (split)	Slices/scan	Voxel size (mm ³)	Description
Gold Data					
IdeaGov [1]	Lesion	119 (95/12/12)	335+82	0.6±0.32	Lung, and COVID-19 related lesions gold standard annotation
MOSMED [27]	Lesion	50 (40/5/5)	41±4	4.29±1.22	COVID-19 related lesions gold standard annotation.
MICCAI-C [28]	Lesion	199 (149/20/20)	69±37	3.03±0.90	COVID-19 related lesions gold standard annotation.
CoronaCases [29]	Lesion	10 (-/-/10)	258±39	0.59±0.15	Lung and COVID-19 lesions gold standard annotation. Test only.
MSC [22]	Separation	9 (7/1/1)	92±116	2.44±0.76	Lung, GGO and consolidation gold standard annotation.
SemiSeg [8]	Separation	100 (45/5/50)	N/A	N/A	COVID-19 GGO and consolidation gold standard annotation. Slices.
ATM [3]	Airway	399 (339/30/30)	663±140	0.33±0.19	Airway gold standard annotation
Parse [4]	Vessel	100 (80/10/10)	303±29	0.46±0.11	Pulmonary Artery gold standard annotation
Silver Data					
IdeaGov [1]	All auto.	1148	399±100	0.54±0.25	COVID-19 CT scans (no manual annotation).
MOSMED [27]	All auto.	848	42±4	4.41±1.00	COVID-19 CT scans (no manual annotation).
Luna16 (LIDC-IDRI) [30]	All auto.	800	256±134	0.78±0.44	Lung cancer CT scans (no manual annotation).
MSD (Lung) [31]	All auto.	50	280±110	0.83±0.30	Lung cancer CT scans (no manual annotation).
Zaffino COVID-19 [32]	All auto.	64	802±185	0.20±0.05	COVID-19 CT scans (no manual annotation).
TCIA Covid 19 [33]	All auto.	457	71±46	2.98±0.89	COVID-19 CT scans (no manual annotation).
NSCLC-Radiomics [34]	All auto.	259	124±22	2.86±0.02	Lung cancer CT scans (no manual annotation).
COVID-19-AR [35]	All auto.	19	552±201	0.84±0.62	COVID-19 CT scans (no manual annotation).
COVID-19-NY-SBU [36]	All auto.	478	228±233	1.64±1.03	COVID-19 CT scans (no manual annotation).
COPD-TLC [37]	All auto.	365	563.26±66.59	0.20±0.04	COPD CT scans (no manual annotation).
Total		6150			

TABLE I

SUMMARY OF GOLD AND SILVER DATA SOURCES WITH THEIR RESPECTIVE NUMBER OF IMAGES AND TRAIN/VAL/TEST SPLITS, MEAN AND STANDARD DEVIATION (STD) OF AXIAL SLICES PER SCAN, VOXEL SIZE (MEAN±STD) AS COMPUTED BY SIMPLEITK [38], AND DESCRIPTION OF THE DATA AND VOXEL-LEVEL ANNOTATIONS IF APPLICABLE. LABEL FORMAT REFERS TO WHAT STRUCTURES ARE ANNOTATED TO WHAT LEVEL OF DETAIL. LESION ANNOTATION HAS HEALTHY AND UNHEALTHY AREA LABELS, SEPARATION HAS HEALTHY, GGO AND CONSOLIDATION AREAS ANNOTATED, AND AIRWAY AND VESSEL ARE BINARY AIRWAY AND PULMONARY ARTERY ANNOTATIONS. SILVER DATA USES AUTOMATED METHODS TO ANNOTATE ALL TARGETS WITH SPECIALIZED nnUNETS, LUNGmask AND SEPARATION THRESHOLDS.

IdeaGov, MOSMED, and MICCAI-C datasets are combined into a development cohort named Lesion representing lesion-level annotations, which was randomly split into 80/10/10 train/validation/testing sets. The combined dataset is highly heterogeneous representing a wide variety of voxel sizes, manufacturers, acquisition parameters, and subtle differences in annotation protocol. SemiSeg, a 2D slice-wise dataset, is separated following the original publication 45/5/50 holdout split [8] and combined with MSC (80/10/10) split into the Separation cohort. CoronaCases is kept as an external lesion test dataset, isolated from development. For datasets containing only lesion annotation, such as MICCAI-C, MOSMED and SemiSeg, lung masks were included with the application of lungmask [12] followed by visual inspection of results.

Finally, ATM and Parse represent airway and pulmonary artery annotations being used in the circulatory branch of MEDSeg and were also split into 80/10/10 holdout splits. For more details on acquisition parameters, please refer to the cited references shown in Table I. All gold datasets are anonymized and were collected outside of the scope of this project, being made available publicly or as part of participation in medical imaging segmentation challenges.

These datasets and splits were also used to train teacher 3D nnUNets [6], which are used to label the silver datasets and for comparison purposes. Teacher nnUNets were separately trained for the following tasks: segmentation of the healthy lung and lesion areas; pulmonary artery segmentation; and airway segmentation.

B. Silver data

Datasets without manual annotation come from a variety of sources with different acquisition parameters and scanners, and were originally collected to study diseases such as chronic obstructive pulmonary disease (COPD), lung cancer, and COVID-19. Note that the subset of MOSMED without annotation is different from the annotated subset in the gold data (Tab. I). Some of these data sources were stored in DICOM format with multiple series and modalities. Therefore, we used a heuristic to automatically select the proper CT axial series with higher resolution and lower noise kernel whenever possible.

All silver scans were used only for training. They were annotated by other automated methods for all targets: Lungmask [12] for whole lung labels, teacher nnUNets [6] for lesion, airway and pulmonary artery, and finally, the lesion area is approximately separated into GGO and consolidation using a -300 HU threshold [21]. All datasets were publicly available with the exception of COPD-TLC, approved under the University of Iowa Institutional Review Board (IRB), consisting of acquisitions of the COPDGene project [37] acquired at the University of Iowa.

C. NORMLD Healthy Control

In addition to the data reported in Table I, the NORMLD dataset collected at the University of Iowa was used as a control dataset. This dataset contains 115 chest CT scans of healthy subjects, permitting evaluation of MEDPSEg’s performance on healthy lungs, whereas all datasets used for training were diseased subjects. The acquisition of this dataset was approved by the University of Iowa IRB.

III. METHODOLOGY

In this section, we go into detail on how the polymorphic MEDPSEg works (Fig. 2), with description of the low level architecture (Section III-A), data preparation (Section III-B), details of how the architecture is optimized in multiple target formats (Sections III-C) and finally our evaluation methodology III-D.

A. Architecture

The original architecture, named CoEDet, has been separately optimized in the past for lung and lesion segmentation in COVID-19, surpassing 3D UNet results [14]. It has also showed good performance in airway segmentation in the ATM challenge [39]. CoEDet works with 2.5D input slices, where each batch sample has 3 axial slices composed of the target slice and its immediate neighbors, regardless of the original spacing. This representation provides local volumetric and slice thickness information. Note, however, in cases where there is no volumetric information (e. g. SemiSeg dataset) the same slice is repeated in the three channels. CoEDet’s output for a given volumetric CT scan is generated by stacking the results of 2.5D predictions in the axial direction for each slice (Fig. 3).

In this work, CoEDet becomes Modified Efficient-Det for Polymorphic Pulmonary Segmentation (MEDPSEg). MEDPSEg uses high-resolution backbone features (starting from $/2$ the original input resolution to $/8$) from an ImageNet pre-trained EfficientNet-B7 [40]. The EfficientNet input stem convolution is replaced with a 3D 3x3 convolution with no padding to take advantage of the 2.5D Input. In a single forward pass, these backbone features are processed by two 128 channel Bidirectional Feature Pyramid Networks (BiFPN) [15], modified with attention gates (BiFPN-AG) at the outputs. The polymorphic BiFPN-AG has polymorphic segmentation heads (PH) with a softmax output of four fixed channels and the circulatory BiFPN-AG has circulatory segmentation heads (CH) with two softmax outputs of two channels each, for multitasking both circulatory targets (Fig 2). Each BiFPN-AG has spatial self-attention gates [19] at its outputs to spatially weight features. Each spatially weighted feature is upsampled (x2), resulting in five multi-scale feature maps from input resolution to $/16$ the original resolution. In the segmentation heads (CH or PH), each feature map is processed by three convolution blocks with separable convolutions [41], batch normalization [42] and swish [43]. The multiple resolution outputs are used for deep supervision [44], where the loss function is applied in places other than the main output to inject gradients into deeper weights more effectively. The contribution to the overall loss L from each of the four deep supervision losses DSL_i for each head is weighted in the following way: $L = 0.75Loss + \sum_{i=1}^4 2^{-(i+2)}DSL_i$ where $Loss$ is the loss of the main high-resolution output. Therefore, 75% of the weight is on the optimization of the main output, and the other 25% is distributed to the optimization of the lower resolution outputs with exponential decay. Whenever MEDPSEg is specialized on a single target format, such as training only for lesion segmentation or only for airway segmentation, only one BiFPN with Attention and Head is used, and this architectural variation is named S-MEDPSEg. Finally, we also explored a parallel approach using a relatively simpler 2.5D AttUNet [19] architecture, with a polymorphic variation P-AttUNet designed by simply having features from a large encoder (1024 channels at bottleneck) used by a main polymorphic decoder and two additional airway and vessel decoders.

B. Data preparation

The heterogeneity of the data, not only in acquisition parameters but also in label format, requires standardization. After careful consideration of different normalization and pre-processing techniques with early experiments, all CT images were clipped to the range $[-1024, 600]$ Hounsfield unit (HU), and then normalized to the range $[0, 1]$. This window contains enough information to contrast both the lung and mediastinal structures in pulmonary CT images. Silver data was cropped to the lung region using Lungmask’s [12] lung segmentation. For gold data, only slices with annotation are used in training. For evaluation, predictions are made on all slices of the input CT image.

For the organization of the annotations, a 4 channel representation was used for every format. This necessity originates

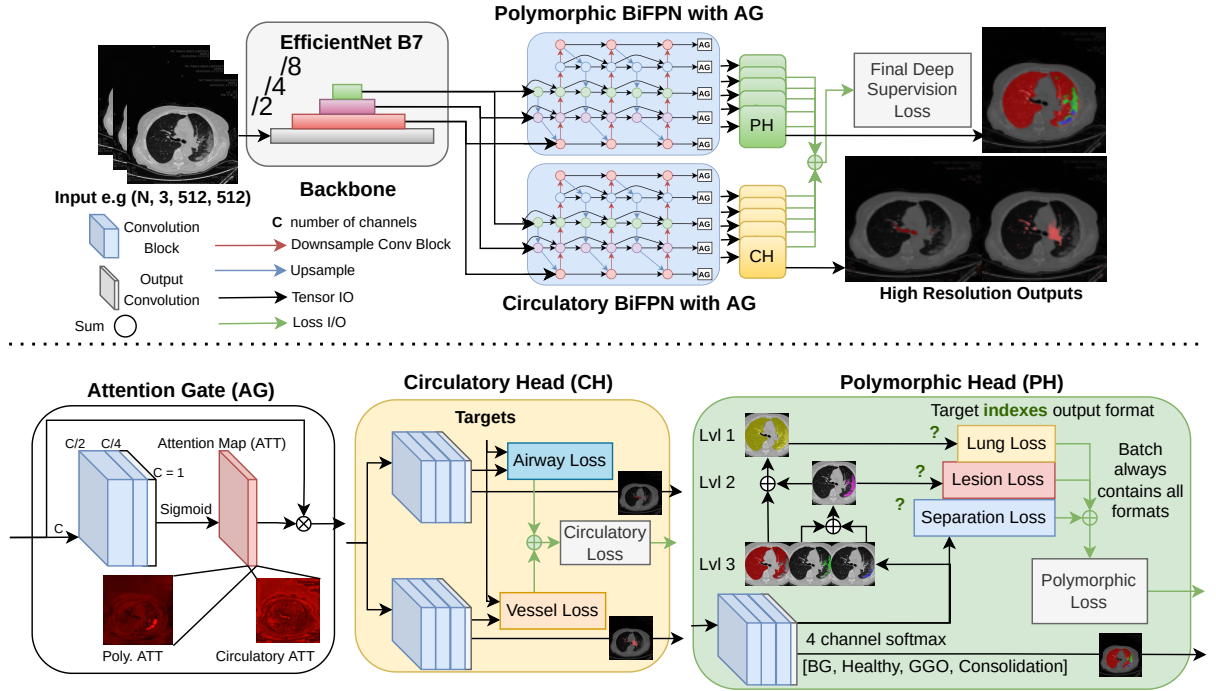


Fig. 2. Illustration of MEDPSeg architecture from initial feature extraction with the EfficientNet backbone to the polymorphic and circulatory head outputs. Multiple output formats are built on the fly with sum reductions and the applicable format is applied depending on the target format of the input image. A batch of images always contains all formats and the final loss always merges training in all annotation formats.

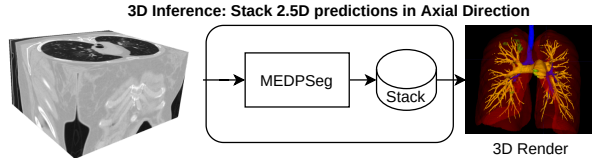


Fig. 3. During validation and for inference, MEDPSeg processes whole volumes through stacking axial predictions.

from the technical limitation of tensors being stored as fixed shape arrays, but we need to have annotations mixed together for proper indexing of the relevant labels. Each slice in a batch can have one of the following target formats: Lung (background: 0, lung: 1); Lesion (background: 0, healthy lung: 1, lesion: 2); Lesion Separation (background: 0, healthy lung: 1, GGO: 2, consolidation: 3); Airway (background: 0, airway: 1); and finally Pulmonary Artery (background: 0, vessel: 1). For silver training, all slices were annotated for all targets with automated methods. Given the different sizes of each dataset, a custom data sampler was implemented to sample and augment each annotation format randomly and ensure every batch has representation from every target format, with 30000 samples per format (lung, lesion, separation, airway, artery) for a total of 150000 samples per epoch. Note that lung samples in this case come from silver data. Each sample is accompanied by metadata indicating the target format. When a target format has less than 30000 annotated samples, such as GGO and consolidation separation or pulmonary artery, we still perform a uniform random sampling, repeating samples. To alleviate this repetition problem, data augmentation is performed on the

fly during training with random scaling and rotation, mirroring of all axis, Gaussian noise, Gaussian blur, brightness and contrast intensity augmentation, and finally a 256×256 random crop. For the target and only for lesion labels, we perform random morphology to try and counter the noisy nature of these annotations. For all cited augmentations we follow the same parameters as Isensee et al.’s 2D nnUNet, sourced from their supplementary material [6].

C. Implementation details

Every batch is properly indexed such that the loss components for each target format are computed separately and summed together. For the polymorphic head, depending on the target format, the fixed four channel output (background, healthy lung, GGO and consolidation) is reduced through sums accordingly to match the target format (Fig 2). Note that this also happens at every deep supervision level. Recall that the derivative of a sum of functions is the sum of the individual derivatives. With this approach, we indirectly propagate gradients to the optimization of all four output channels even when the target doesn’t contain that information directly, but a suitable prediction can be built by summing the relevant outputs together. For example, a lesion prediction can be built by summing the GGO and consolidation outputs, and the whole lung can be built by summing the lesion with the healthy lung output. This approach allows us to merge large datasets with more readily available simpler labels with smaller datasets with more complex manual labels while always optimizing the four output channels. In addition, a multitasking branch for airway and vessel segmentation is also

included, to test if additional multitasking will lead to further improved results.

The final *Loss* for optimization is computed by aggregating the contribution from all target formats:

$$Loss = \frac{L_{airway} + L_{vessel} + L_{lung} + L_{lesion} + L_{separation}}{5} \quad (1)$$

For every component of *Loss*, let the underlying loss function be L , with 0-indexed channel c of a total of C channels and corresponding softmax output segmentation \hat{y}_c and target segmentation y_c . L is the sum of generalized dice loss (GDL) [17], without background, and cross entropy loss with background: $L = GDL(\hat{y}, y) + CrossEntropyLoss(\hat{y}, y)$.

The intent is to leverage different aspects of both such as the dynamic weight of GDL. In GDL, a channel contribution is inversely proportional to its area, reducing the effects of class imbalance in small targets. On the other hand, cross-entropy penalizes errors more heavily and includes background optimization. Additional hyperparameters involved in our best result are AdamW as the optimizer with initial learning rate $1e-4$ and weight decay $1e-5$; exponential learning rate decay of 0.985; and, for gold training, batch size of 25 (5 from each target format). Some experiments to arrive at these parameters are reported in [45]. Note that the best weight is selected by the lower validation loss over 3D scans, with a volumetric output being built on-the-fly by stacking predictions. We select the best validation loss weight after 120 hours (approximately 50 epochs when including all data) of training in a A100 80GB GPU or 3080Ti 12 GB GPU, depending on the memory requirements of the experiment. The same parameters are used in silver and gold training, with the exception that silver training uses batch size 1 of one 512x512 fully (silver data) annotated slice. Full open source implementation is available at <https://github.com/MICLab-Unicamp/medseg>.

D. Evaluation

The following quantitative evaluation metrics are employed in this work: firstly, Dice [17], false positive error (FPE) and false negative error (FNE) are used as implemented by SimpleITK [38]. FNE represents the rate at which positive voxels were classified as negative, and is also equal to $1 - Sensitivity$. FPE represents the rate of positive predictions that were false positives. Higher FPE and FNE represent worse performance. Note that SimpleITK’s definition of FPE does not include the number of negative voxels and subsequently has no bias to increased field of view or smaller segmentations, a problem that happens with specificity and other implementations of FPE. Finally, Dice is used as a general overlap metric that takes into account both false positives and false negatives. Note, however, that Dice tends to assume a higher value in large structures, such as for the lung parenchyma, and the larger the structure, the less perceptible the penalization due to small errors [46]. In addition, since lesions are not always present, a special case needs to be established as follows: when no target or prediction is present, the Dice is assumed to be 1. When a metric is by definition not

defined, such as sensitivity without positive cases, that specific case is not considered for that metric computation. Finally, whenever results are compared in terms of significance, the Wilcoxon signed-rank test with $p < 0.05$ is used [47]. Note that these overlap and voxel-wise metrics are not sufficient for evaluating tubular segmentation tasks, and we adopt the tree length detected rate (TD) and branch detected rate (BD) of the largest connected component, as implemented by the evaluation pipeline from the ATM22 airway segmentation challenge [3]. Overall, metrics are computed with 3D targets and predictions, except for comparisons with other methods in the 2D SemiSeg dataset, where the same metrics as the original publications are used, namely slice-wise Dice, specificity and sensitivity [8].

IV. EXPERIMENTS AND RESULTS

In this section, we report the results of experiments performed to assess the performance of MEDPSeg, from justifying hyperparameter choices starting with a baseline S-MEDSeg architecture for lesion separation to transitioning into verifying the impact of polymorphic training and multitasking. Finally, our best polymorphic method (MEDPSeg) is compared with other methods in all segmentation targets and we report quantitative, qualitative, and reproducibility results. For all experiments, unless noted otherwise, the parameters detailed in Section III are used.

A. GGO and consolidation separation

In this experiment, we explored training S-MEDSeg variations only on scarce gold data GGO and consolidation labels from the Separation cohort. Testing uses the SemiSeg testing data, with models also being tested in a reduction to the Lesion cohort test split. To test in lesion data, the GGO and consolidation outputs are reduced with a sum operation into a general lesion label. These experiments studied the impact of backbone size, different loss functions and the addition of deep supervision and self-attention in both performance in the separation test and generalization capabilities to the general lesion labels (Tab. II). When not using deep supervision, BiFPN outputs are upsampled and summed together to the highest resolution. A reference 2.5D AttUNet run was also included in this ablation to verify the benefit of using the S-MEDSeg architecture.

Experiment 1 revealed the benefits of increasing backbone size and our architecture in relation to a baseline Attention UNet. Deep supervision with attention also appears to improve results and generalization capabilities to the more general Lesion segmentation task. In addition, the Cross Entropy + GDL loss approach also results in more performing and balanced models in terms of generalization to lesion labels when training in separation labels.

B. Polymorphic Training and Multitasking

An ablation study was performed to evaluate the contribution of components of the proposed polymorphic model (MEDPSeg). Different models were trained using only gold

Method	Loss	DS	SA	GGO (2D Dice)	Con. (2D Dice)	Lesion (Dice)
B4 S-MEDSeg	GDL	No	No	0.64 ± 0.18	0.32 ± 0.25	0.44 ± 0.22
B4 S-MEDSeg	Focal	No	No	0.30 ± 0.27	0.22 ± 0.41	0.10 ± 0.12
B4 S-MEDSeg	Tversky	No	No	0.66 ± 0.17	0.45 ± 0.29	0.37 ± 0.24
B4 S-MEDSeg	CE + GDL	No	No	0.57 ± 0.23	0.44 ± 0.29	0.24 ± 0.18
AttUNet [19]	CE + GDL	No	Yes	0.58 ± 0.21	0.46 ± 0.29	0.37 ± 0.24
B7 S-MEDSeg	Tversky	No	No	0.66 ± 0.17	0.46 ± 0.29	0.45 ± 0.23
B7 S-MEDSeg	Tversky	Yes	Yes	0.67 ± 0.16	0.46 ± 0.28	0.18 ± 0.22
B7 S-MEDSeg	CE + GDL	No	No	0.65 ± 0.18	0.47 ± 0.29	0.43 ± 0.20
2D nnUNet [6]	CE + Dice	Yes	No	0.65 ± 0.22	0.50 ± 0.32	0.42 ± 0.24
B7 S-MEDSeg	CE + GDL	Yes	Yes	0.66 ± 0.16	0.50 ± 0.29	0.46 ± 0.21

TABLE II

EXPERIMENTS SCALING UP THE SIZE OF THE BACKBONE EFFICIENTNET, TESTING DIFFERENT LOSS FUNCTIONS AND THE IMPACT OF DEEP SUPERVISION WITH SELF ATTENTION (DS/SA), INCLUDING REFERENCE PERFORMANCE FROM AN ATTENTION UNET AND 2D nnUNET. GGO AND CONSOLIDATION (CON.) DICE ARE COMPUTED ON THE SEMISEG TEST DATASET AND LESION DICE IS COMPUTED ON THE LESION COHORT TEST SET. BEST RESULT IN BOLD.

data, in each model one of the following components was removed: data augmentation, deep supervision, and airway and pulmonary artery segmentation tasks. In addition, the performance of MEDPSEg is assessed while: only trained with lower quality silver data with all target formats; only trained with gold data; and finally the performance of pre-training with silver data and then training with gold data after seeing all silver data once (Tab. III). When introducing gold data, silver data is still present but only as the polymorphic level 1 (lung) label (Fig 2). This approach avoids the “forgetfulness” effect [48] regarding the CT scan variety included in the silver data.

Description	Airway (Dice)	Vessel (Dice)	Lesion (Dice)	GGO (2D Dice)	Con. (2D Dice)
Airway SM	0.92 ± 0.04	N/A	N/A	N/A	N/A
Vessel SM	N/A	0.85 ± 0.03	N/A	N/A	N/A
Lesion SM	N/A	N/A	0.66 ± 0.21	N/A	N/A
GGO/Con. SM	N/A	N/A	0.46 ± 0.21	0.66 ± 0.16	0.50 ± 0.29
No aug.	0.88 ± 0.05	0.79 ± 0.04	0.55 ± 0.27	0.48 ± 0.22	0.15 ± 0.19
No DS	0.83 ± 0.09	0.84 ± 0.03	0.62 ± 0.20	0.61 ± 0.24	0.49 ± 0.31
No Airway/PA	N/A	N/A	0.63 ± 0.22	0.57 ± 0.27	0.55 ± 0.29
Silver data	0.61 ± 0.20	0.74 ± 0.05	0.40 ± 0.28	0.60 ± 0.19	0.22 ± 0.41
P-AttUNet	0.88 ± 0.05	0.84 ± 0.03	0.63 ± 0.20	0.63 ± 0.21	0.57 ± 0.28
Gold data	0.90 ± 0.04	0.84 ± 0.04	0.64 ± 0.22	0.61 ± 0.23	0.58 ± 0.31
Silver > gold	0.90 ± 0.05	0.88 ± 0.02	0.66 ± 0.20	0.65 ± 0.20	0.58 ± 0.29

TABLE III

MEDPSEg POLYMORPHIC TRAINING EXPERIMENTS TEST RESULTS. RESULTS FOR SPECIALIZED S-MEDSEG (SM) FOR EACH TARGET FORMAT ARE INCLUDED FOR COMPARISON. MODIFIED PARAMETERS INCLUDE DISABLING DEEP SUPERVISION (DS) OR AUGMENTATION (AUG.), NOT USING AIRWAY AND PULMONARY ARTERY (PA) TARGETS, TRAINING ONLY WITH SILVER DATA, ONLY WITH GOLD DATA IN MEDPSEg AND WITH A POLYMORPHIC ATTUNET VARIATION, AND TUNING (>) THE SILVER-TRAINED WEIGHTS TO GOLD DATA. N/A REFERS TO THE MODEL NOT BEING APPLICABLE TO THE TARGET FORMAT. TOP TWO RESULTS IN BOLD.

Results show that deep supervision, augmentation, and inclusion of pulmonary structure targets (airway and pulmonary artery) are essential for the best performance of MEDPSEg in lesions, GGO, and consolidations. Initial training with silver data and subsequent training with gold data mixed with silver lungs achieved the best overall performance. Note that the convergence of MEDPSEg is relatively difficult. We were not able to achieve proper loss convergence in all targets while using a 3D Polymorphic AttUNet or 3D MEDPSEg variation. In addition, there was a need to separate the vessel and airway

outputs on the circulatory head for best results. A single three-channel softmax had poor performance in comparison to two, two-channel, softmax outputs.

C. Comparisons with other methods

To show the performance of our best MEDPSEg model against other methods from the literature which are specialized in each of the targets MEDPSEg outputs. MEDPSEg is also evaluated against Lungmask in lung parenchyma segmentation in the IdeiaGov test data, containing severe pneumonia cases with a median lung involvement of approximately 40%. Comparisons are done with specialized 3D nnUNets (2021) trained separately in the same vessel, airway and lesion training data. For other included methods such as COPLE-Net (2020) [16], Biondi et al. (2021) [49], Lungmask (2020) [12], AMFM (2006) [50], Zheng et al. (2021) [51], we reproduced their prediction capabilities with the provided trained weights and/or implementation code and used the same evaluation implementation for all methods. Note that these methods used different training data. Separate boxplots showcase Dice, FPE and FNE for each target format. All MEDPSEg results are from the same trained weights (Fig. 4).

AMFM and Biondi et al. are based on traditional feature engineering machine learning and have significantly lower lesion segmentation performance than MEDPSEg. There is no statistically significant Dice difference between MEDPSEg and the compared deep learning-based methods specialized in Lesion and Vessel segmentation. When looking at proper largest connected tubular component segmentation metrics, MEDPSEg performs comparably to specialized nnUNets in the circulatory targets. For airway segmentation, MEDPSEg achieved 84.15 ± 8.14 BD (%) and 91.45 ± 3.92 TD (%), nnUNet achieved 84.16 ± 8.77 BD (%) and 90.82 ± 5.19 TD (%), and Zheng et al. [51] achieved 71.59 ± 15.89 BD and 83.63 ± 9.12 TD. For pulmonary artery segmentation, MEDPSEg achieved 82.47 ± 9.32 BD (%) and 90.78 ± 4.25 TD (%) and nnUNet achieved 83.24 ± 12.45 BD (%) and 91.31 ± 5.96 TD (%). MEDPSEg performed significantly better in lung parenchyma segmentation of severe pneumonia patients than Lungmask [12]. Finally, to assess GGO and consolidation performance, MEDPSEg is compared to other methods in the literature in the 2D SemiSeg test set. (Tab. IV).

Dataset	SemiSeg						
	Target	GGO			Consolidation		
Method		Dice	Sen.	Spec.	Dice	Sen.	Spec.
InfNet [8]		0.62	0.62	0.97	0.46	0.51	0.97
mmVitSeg [9]		0.63	0.66	0.96	0.35	0.36	0.70
Jin et al. [52]		0.59	0.61	0.96	0.32	0.33	0.76
2D nnUNet [6]		0.65	0.60	0.99	0.50	0.46	0.99
TV-Unet [53]		0.65	0.76	0.98	0.54	0.56	0.99
MEDPSEg		0.65	0.64	0.99	0.58	0.54	0.99

TABLE IV

OUR BEST POLYMORPHIC MEDPSEg COMPARED ON THE SEMISEG TEST DATASET WITH SLICE-WISE MEAN METRICS DICE, SENSITIVITY (SEN.) AND SPECIFICITY (SPEC.) AS REPORTED BY OTHER METHODS FROM THE LITERATURE. TOP RESULTS IN BOLD.

When looking at the challenging problem of GGO and consolidation separation (Fig 5), with limited availability of

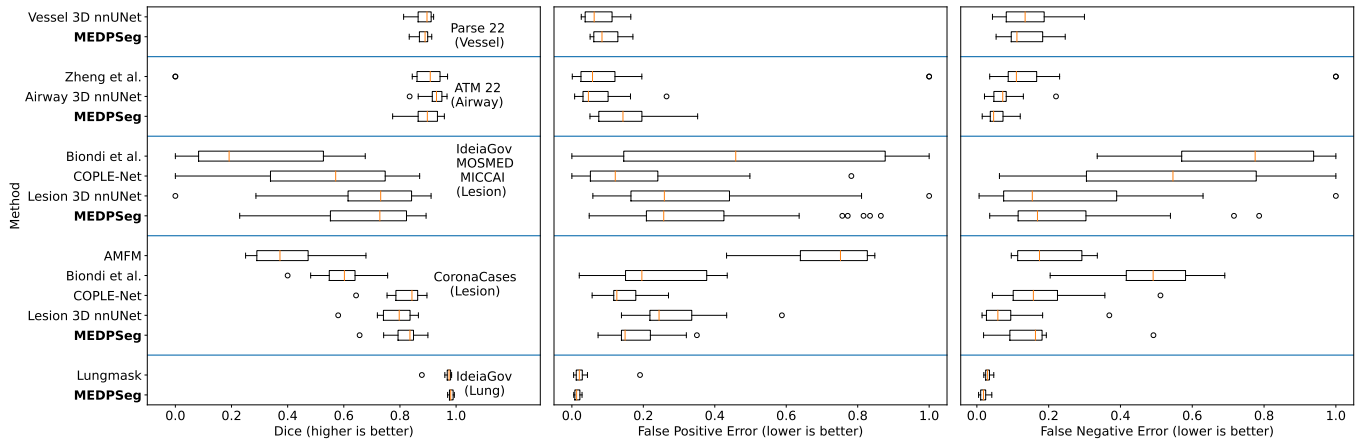


Fig. 4. Boxplots of Dice, FPE and FNE with the same best MEDPSeg in bold compared to multiple state-of-the-art methods in different targets.

annotated data, the proposed method outperforms multiple recent works achieving state-of-the-art GGO and consolidation performance in the SemiSeg test dataset, with significantly better Dice on consolidation. For both GGO and consolidation performance, MEDPSeg is the best-performing method.

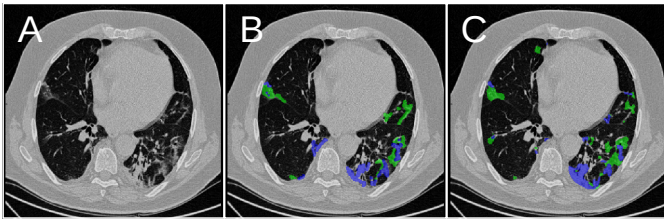


Fig. 5. A test case from SemiSeg dataset showing (A) axial CT slice, (B) groundtruth, and (C) MEDPSeg prediction, with GGO in green and consolidations in blue.

Finally, after running MEDPSeg in 115 healthy control subjects, the mean lung involvement by GGO is of $0.12 \pm 0.16\%$, with $0.0009 \pm 0.003\%$ consolidation involvement, showcasing MEDPSegs low false positive rate. For comparison, AMFM detects $0.31 \pm 0.19\%$ of overall lesion involvement and nnUNet found 0.02 ± 0.04 and 0.008 ± 0.03 of GGO and consolidation involvement respectively. Note that these values are less than 1% and it is possible for healthy subjects to have a small amount of benign opacities [54].

In general, when compared to other methods, MEDPSeg simultaneously segments multiple pulmonary targets with comparable or better performance to specialized state-of-the-art methods. It achieves superior performance compared to current state-of-the-art for segmentation of GGO, consolidation, and lung parenchyma with severe pneumonia. MEDPSeg performs segmentation of all targets simultaneously in a single forward pass of one network and does not require any post-processing other than stacking axial predictions. As a result, MEDPSeg is able to provide a complete high-resolution 3D pulmonary segmentation in less than 1 minute with a NVidia 2060 GPU. Even without considering the logistical difficulty of training and using separate specialized methods for each target, one can achieve five times faster prediction on average with MEDPSeg

in comparison to performing inference with five separately trained methods.

Figure 6 shows 3D renderings of a high-resolution contrast enhanced CT from MEDPSeg compared to specialized segmentations from different nnUNets and Lungmask. MEDPSeg can provide all these different labels with a low resource usage footprint and robust generalization capabilities both in low and high-resolution scans due to its 2.5D nature and its training data variability.

D. Reproducibility

An important consideration of MEDPSeg’s development was implementing a lightweight reproducibility tool as a python pip package in parallel, with a graphical user interface, designed for ease of use by both experts and non-experts in the medical or engineering fields. Open source code and trained weights for reproducing our segmentation capabilities are in <https://github.com/MICLab-Unicamp/medseg>. The only requirement for usage of the tool is a Python pip or conda environment. Due to working in a slice-wise manner, MEDPSeg can run in relatively low computer specifications for fast performance of less than 1 minute per high-resolution scan. Usage of the tool can be resumed to selecting a folder or CT scan file and selecting the output location for all segmentations masks, volume statistics, and lung involvement reports separated by lung and lobe.

V. DISCUSSION

The same MEDPSeg model is statistically similar or significantly better in overlap metrics than MEDSeg and nnUNets trained separately to predict each target independently. Of note is the statistically significant improvement in consolidation separation and lung parenchyma with high opacity involvement. Overall, these results confirm the importance of data variability and correct data processing during training of medical imaging segmentation models [6]. The usage of pre-training with silver data labels proved to be important in achieving MEDPSeg’s high performance. Interestingly, including the airway and pulmonary artery segmentation task during training increased performance of lung lesion segmentation.

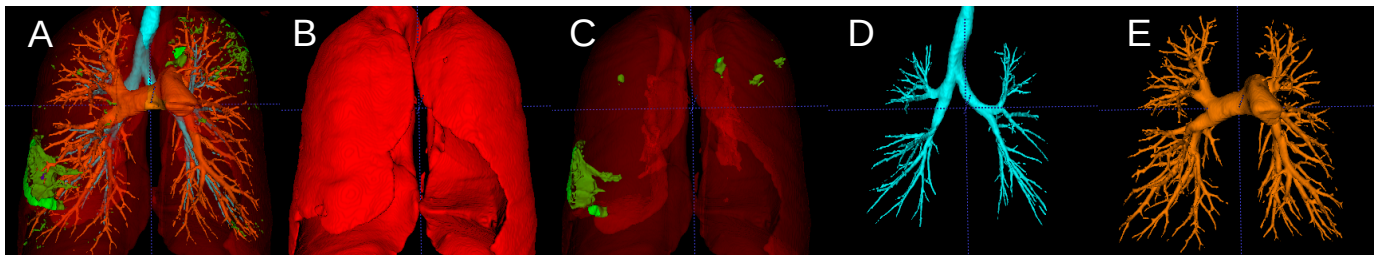


Fig. 6. (A) A 3D rendering of MEDPSeg prediction and comparison to other specialized methods, including: (B) Lungmask, (C) lesion trained nnUNet, (D) airway trained nnUNet, and (E) vessel trained nnUNet. All results were computed on the same CT scan.

Improvements from multitask learning are well-known in the literature [55]. However, MEDPSeg’s results show the additional potential of using polymorphic learning and the hierarchical property of medical imaging data to optimize targets with low availability of annotation. Polymorphic learning allows one to mix target data of different formats from different datasets. A similar methodology could be applied to other problems which have labels with hierarchical structure with varying degrees of specificity. This results in more data variability in training and allows for indirect optimization of complex targets while leveraging more readily available simpler targets. We have demonstrated this in the task of lesion segmentation and separation into GGO and consolidation.

MEDPSeg is not without limitations. MEDPSeg will still try to predict vessels and airways in scans with high distance between slices but results will not be correct due to these structures not being visible in low resolution CT. For this reason, silver data circulatory annotation was not entirely useful in improving circulatory results as seen in experiments. Moreover, gold training samples for pulmonary artery segmentation were contrast-enhanced CTs, meaning in scans without contrast pulmonary artery results outside of the lung will be of lower quality due to low mediastinal contrast. Another limitation is the difficulty of implementation of the training process, regarding data preparation, balancing of the batch, and the computation of loss for each target format, requiring custom implementation for each problem. However, the reproducibility of the prediction capabilities of trained MEDPSeg is easily available in our online repository.

VI. CONCLUSION

This work proposes MEDPSeg, a new methodology and architecture which leverages information from datasets with conflicting manual and automated target formats, using polymorphic and multitask training to achieve state-of-the-art performance in multiple chest CT segmentation tasks. We showcase how one could use the hierarchical properties of the lung anatomy and its internal lesions to indirectly optimize the segmentation of detailed targets while mixing in simpler and more readily available general lesion and lung annotation. Moreover, benefits of including circulatory and airway targets are demonstrated. Finally, we provide open-source trained weights and easy-to-use graphical tool for the reproducibility of MEDPSeg’s segmentation capabilities. We hope for MEDPSeg to be used to reliably characterize large chest CT cohorts in future studies.

REFERENCES

- [1] D. Carmo, I. Campiotti, L. Rodrigues, I. Fantini, G. Pinheiro, D. Moraes, R. Nogueira, L. Rittner, and R. Lotufo, “Rapidly deploying a COVID-19 decision support system in one of the largest Brazilian hospitals,” *Health Informatics J.*, vol. 27, no. 3, p. 14604582211033017, 2021.
- [2] D. Carmo, R. Tudas, A. Comellas, A. Pezzullo, R. Villacreses, J. Cho, J. Zabner, L. Rittner, R. Lotufo, J. Reinhardt *et al.*, “Evidence of post-infection vaccination correlation with the severity of opacities and consolidations on the lung parenchyma of post-acute SARS-CoV-2 patients,” in *D95. CHALLENGES AND ADVANCES IN COVID-19*. American Thoracic Society, 2023, pp. A6579–A6579.
- [3] M. Zhang, Y. Wu, H. Zhang, Y. Qin, H. Zheng, W. Tang, C. Arnold, C. Pei, P. Yu, Y. Nan *et al.*, “Multi-site, multi-domain airway tree modeling,” *Med. Image Anal.*, p. 102957, 2023.
- [4] G. Luo, K. Wang, J. Liu, S. Li, X. Liang, X. Li, S. Gan, W. Wang, S. Dong, W. Wang *et al.*, “Efficient automatic segmentation for multi-level pulmonary arteries: The parse challenge,” *arXiv preprint arXiv:2304.03708*, 2023.
- [5] O. Ronneberger, P. Fischer, and T. Brox, “U-net: Convolutional networks for biomedical image segmentation,” in *Intl. Conf. on Med. Image. Comput. Comput. Assist. Interv. (MICCAI)*. Springer, 2015, pp. 234–241.
- [6] F. Isensee, P. F. Jaeger, S. A. Kohl, J. Petersen, and K. H. Maier-Hein, “nnU-Net: a self-configuring method for deep learning-based biomedical image segmentation,” *Nat. methods*, vol. 18, no. 2, pp. 203–211, 2021.
- [7] D. Carmo, J. Ribeiro, S. Dertkigil, S. Appenzeller, R. Lotufo, and L. Rittner, “A systematic review of automated segmentation methods and public datasets for the lung and its lobes and findings on computed tomography images,” *Yearb. Med. Informatics*, vol. 31, no. 01, pp. 277–295, 2022.
- [8] D.-P. Fan, T. Zhou, G.-P. Ji, Y. Zhou, G. Chen, H. Fu, J. Shen, and L. Shao, “Inf-net: Automatic COVID-19 lung infection segmentation from CT images,” *IEEE Trans. on Med. Imaging*, 2020.
- [9] Y. Yang, L. Zhang, L. Ren, and X. Wang, “Mmvit-seg: A lightweight transformer and cnn fusion network for COVID-19 segmentation,” *Comput. Methods Programs Biomed.*, vol. 230, p. 107348, 2023.
- [10] M. Roberts, D. Driggs, M. Thorpe, J. Gilbey, M. Yeung, S. Ursprung, A. I. Aviles-Rivero, C. Etmann, C. McCague, L. Beer *et al.*, “Common pitfalls and recommendations for using machine learning to detect and prognosticate for COVID-19 using chest radiographs and CT scans,” *Nat. Mach. Intell.*, vol. 3, no. 3, pp. 199–217, 2021.
- [11] A. Khan, S. H. Khan, M. Saif, A. Batoool, A. Sohail, and M. Waleed Khan, “A survey of deep learning techniques for the analysis of COVID-19 and their usability for detecting omicron,” *J. Exp. & Theor. Artif. Intell.*, pp. 1–43, 2023.
- [12] J. Hofmanninger, F. Prayer, J. Pan, S. Röhrich, H. Prosch, and G. Langs, “Automatic lung segmentation in routine imaging is primarily a data diversity problem, not a methodology problem,” *Eur. Radiol. Exp.*, vol. 4, no. 1, pp. 1–13, 2020.
- [13] H. R. Roth, Z. Xu, C. Tor-Díez, R. S. Jacob, J. Zember, J. Molto, W. Li, S. Xu, B. Turkbey, E. Turkbey *et al.*, “Rapid artificial intelligence solutions in a pandemic—the covid-19-20 lung CT lesion segmentation challenge,” *Med. image analysis*, vol. 82, p. 102605, 2022.
- [14] D. Carmo, I. Campiotti, I. Fantini, L. Rodrigues, L. Rittner, and R. Lotufo, “Multitasking segmentation of lung and COVID-19 findings in CT scans using modified EfficientDet, UNet and MobileNetV3 models,” in *17th Intl. Symp. on Med. Info. Proc. and Anal. (SIPAIM)*, vol. 12088. SPIE, 2021, pp. 65–74.

- [15] M. Tan, R. Pang, and Q. V. Le, "Efficientdet: Scalable and efficient object detection," in *Proc. IEEE Conf. Comput. Vis. Pattern Recognit. (CVPR)*, 2020, pp. 10781–10790.
- [16] G. Wang, X. Liu, C. Li, Z. Xu, J. Ruan, H. Zhu, T. Meng, K. Li, N. Huang, and S. Zhang, "A noise-robust framework for automatic segmentation of COVID-19 pneumonia lesions from CT images," *IEEE Trans. on Med. Imaging*, vol. 39, no. 8, pp. 2653–2663, 2020.
- [17] C. H. Sudre, W. Li, T. Vercauteren, S. Ourselin, and M. J. Cardoso, "Generalised dice overlap as a deep learning loss function for highly unbalanced segmentations," in *Deep learning in med. image anal. and multimodal learning for clin. decision support (DLMIA)*. Springer, 2017, pp. 240–248.
- [18] L. Henschel, S. Conjeti, S. Estrada, K. Diers, B. Fischl, and M. Reuter, "Fastsurfer-a fast and accurate deep learning based neuroimaging pipeline," *NeuroImage*, vol. 219, p. 117012, 2020.
- [19] D. Carmo, L. Rittner, and R. de Alencar Lotufo, "Multiattuned: Brain tumor segmentation and survival multitasking," in *BrainLes@ MICCAI (1)*, 2020, pp. 424–434.
- [20] Z. Tan, J. Feng, and J. Zhou, "Sgnet: Structure-aware graph-based network for airway semantic segmentation," in *Intl. Conf. on Med. Image. Comput. Comput. Assist. Interv. (MICCAI)*. Springer, 2021, pp. 153–163.
- [21] W. Lu, J. Wei, T. Xu, M. Ding, X. Li, M. He, K. Chen, X. Yang, H. She, and B. Huang, "Quantitative CT for detecting COVID-19 pneumonia in suspected cases," *BMC Infect. Dis.*, vol. 21, no. 1, pp. 1–8, 2021.
- [22] MedSeg, "COVID-19 CT segmentation dataset (nr. 2)," <http://medicalsegmentation.com/covid19/>, 2020, [Online; accessed 28-July-2021].
- [23] L. Li, T. Zhou, W. Wang, J. Li, and Y. Yang, "Deep hierarchical semantic segmentation," in *Proc. IEEE Conf. Comput. Vis. Pattern Recognit. (CVPR)*, 2022, pp. 1246–1257.
- [24] S. Bakas, M. Reyes, A. Jakab, S. Bauer, M. Rempfler, A. Crimi, R. T. Shinohara, C. Berger, S. M. Ha, M. Rozycki *et al.*, "Identifying the best machine learning algorithms for brain tumor segmentation, progression assessment, and overall survival prediction in the brats challenge," *arXiv preprint arXiv:1811.02629*, 2018.
- [25] S. E. Gerard, J. Herrmann, Y. Xin, K. T. Martin, E. Rezoagli, D. Ippolito, G. Bellani, M. Cereda, J. Guo, E. A. Hoffman, D. W. Kaczka, and J. M. Reinhardt, "CT image segmentation for inflamed and fibrotic lungs using a multi-resolution convolutional neural network," *Sci. reports*, vol. 11, no. 1, pp. 1–12, 2021.
- [26] P. A. Yushkevich, J. Piven, H. C. Hazlett, R. G. Smith, S. Ho, J. C. Gee, and G. Gerig, "User-guided 3d active contour segmentation of anatomical structures: significantly improved efficiency and reliability," *Neuroimage*, vol. 31, no. 3, pp. 1116–1128, 2006.
- [27] S. P. Morozov, A. Andreychenko, N. Pavlov, A. Vladzmyrskyy, N. Ledikhova, V. Gomboleviskiy, I. A. Blokhin, P. Gelezhe, A. Gonchar, and V. Y. Chernina, "Mosmeddata: Chest CT scans with COVID-19 related findings dataset," *arXiv preprint arXiv:2005.06465*, 2020.
- [28] H. Roth, Z. Xu, C. T. Diez, R. S. Jacob, J. Zember, J. Molto, W. Li, S. Xu, B. Turkbey, E. Turkbey *et al.*, "Rapid artificial intelligence solutions in a pandemic-the covid-19-20 lung CT lesion segmentation challenge," *Res. Sq. Prepr.*, 2021.
- [29] J. P. Cohen, P. Morrison, L. Dao, K. Roth, T. Q. Duong, and M. Ghassemi, "COVID-19 image data collection: Prospective predictions are the future," *arXiv 2006.11988*, 2020. [Online]. Available: <https://github.com/ieee8023/covid-chestxray-dataset>
- [30] A. A. A. Setio, A. Traverso, T. De Bel, M. S. Berens, C. Van Den Bogaard, P. Cerello, H. Chen, Q. Dou, M. E. Fantacci, B. Geurts *et al.*, "Validation, comparison, and combination of algorithms for automatic detection of pulmonary nodules in computed tomography images: the luna16 challenge," *Med. image analysis*, vol. 42, pp. 1–13, 2017.
- [31] M. Antonelli, A. Reinke, S. Bakas, K. Farahani, A. Kopp-Schneider, B. A. Landman, G. Litjens, B. Menze, O. Ronneberger, R. M. Summers *et al.*, "The medical segmentation decathlon," *Nat. communications*, vol. 13, no. 1, p. 4128, 2022.
- [32] P. Zaffino, A. Marzullo, S. Moccia, F. Calimeri, E. De Momi, B. Bertucci, P. P. Arcuri, and M. F. Spadea, "An open-source COVID-19 CT dataset with automatic lung tissue classification for radiomics," *Bioengineering*, vol. 8, no. 2, p. 26, 2021.
- [33] P. An, S. Xu, S. A. Harmon, E. B. Turkbey, T. H. Sanford, A. Amalou, M. Kassim, N. Varble, M. Blain, V. Anderson *et al.*, "Ct images in COVID-19 [data set]," *The Cancer Imaging Arch.*, vol. 10, 2020.
- [34] H. J. Aerts, E. R. Velazquez, R. T. Leijenaar, C. Parmar, P. Grossmann, S. Carvalho, J. Bussink, R. Monshouwer, B. Haibe-Kains, D. Rietveld *et al.*, "Decoding tumour phenotype by noninvasive imaging using a quantitative radiomics approach," *Nat. communications*, vol. 5, no. 1, p. 4006, 2014.
- [35] S. Desai, A. Baghal, T. Wongsurawat, P. Penjaroenpun, T. Powell, S. Al-Shukri, K. Gates, P. Farmer, M. Rutherford, G. Blake *et al.*, "Chest imaging representing a COVID-19 positive rural us population," *Sci. data*, vol. 7, no. 1, p. 414, 2020.
- [36] J. Saltz, M. Saltz, P. Prasanna, R. Moffitt, J. Hajagos, E. Bremer, J. Balsamo, and T. Kurc, "Stony brook university COVID-19 positive cases," *cancer imaging archive*, vol. 4, 2021.
- [37] E. A. Regan, J. E. Hokanson, J. R. Murphy, B. Make, D. A. Lynch, T. H. Beaty, D. Curran-Everett, E. K. Silverman, and J. D. Crapo, "Genetic epidemiology of copd (copdgene) study design," *COPD: J. Chronic Obstr. Pulm. Dis.*, vol. 7, no. 1, pp. 32–43, 2011.
- [38] R. Beare, B. Lowekamp, and Z. Yaniv, "Image segmentation, registration and characterization in r with simpleitk," *J. statistical software*, vol. 86, 2018.
- [39] D. Carmo, L. Rittner, and R. Lotufo, "Open-source tool for airway segmentation in computed tomography using 2.5 d modified efficientdet: Contribution to the atm22 challenge," *arXiv preprint arXiv:2209.15094*, 2022.
- [40] M. Tan and Q. V. Le, "Efficientnet: Rethinking model scaling for convolutional neural networks," *arXiv preprint arXiv:1905.11946*, 2019.
- [41] F. Chollet, "Xception: Deep learning with depthwise separable convolutions," in *Proc. IEEE Conf. Comput. Vis. Pattern Recognit. (CVPR)*, 2017, pp. 1251–1258.
- [42] S. Ioffe and C. Szegedy, "Batch Normalization: Accelerating Deep Network Training by Reducing Internal Covariate Shift," *arXiv:1502.03167 [cs]*, Mar. 2015, arXiv: 1502.03167. [Online]. Available: <http://arxiv.org/abs/1502.03167>
- [43] P. Ramachandran, B. Zoph, and Q. V. Le, "Searching for activation functions," *arXiv preprint arXiv:1710.05941*, 2017.
- [44] L. Wang, C.-Y. Lee, Z. Tu, and S. Lazebnik, "Training deeper convolutional networks with deep supervision," *arXiv preprint arXiv:1505.02496*, 2015.
- [45] D. S. Carmo, R. A. Tudas, A. P. Comellas, L. Rittner, R. A. Lotufo, J. M. Reinhardt, and S. E. Gerard, "Automatic segmentation of lung findings in CT and application to long COVID," *arXiv preprint arXiv:2310.09446*, 2023.
- [46] L. Maier-Hein, B. Menze *et al.*, "Metrics reloaded: Pitfalls and recommendations for image analysis validation," *arXiv.org*, no. 2206.01653, 2022.
- [47] D. Carmo, G. Pinheiro, L. Rodrigues, T. Abreu, R. Lotufo, and L. Rittner, "Automated computed tomography and magnetic resonance imaging segmentation using deep learning: a beginner's guide," *arXiv preprint arXiv:2304.05901*, 2023.
- [48] A. Cossu, T. Tuytelaars, A. Carta, L. Passaro, V. Lomonaco, and D. Bacciu, "Continual pre-training mitigates forgetting in language and vision," *arXiv preprint arXiv:2205.09357*, 2022.
- [49] R. Biondi, N. Curti, F. Coppola, E. Giampieri, G. Vara, M. Bartoletti, A. Cattabriga, M. A. Coccozza, F. Ciccarese, C. De Benedittis, L. Cerenelli, B. Bortolani, E. Marcelli, L. Pierotti, L. Strigari, P. Viale, R. Golfieri, and G. Castellani, "Classification performance for covid patient prognosis from automatic ai segmentation—a single-center study," *Appl. Sci.*, vol. 11, no. 12, 2021. [Online]. Available: <https://www.mdpi.com/2076-3417/11/12/5438>
- [50] Y. Xu, M. Sonka, G. McLennan, J. Guo, and E. A. Hoffman, "Mdct-based 3-d texture classification of emphysema and early smoking related lung pathologies," *IEEE Trans. on Med. Imaging*, vol. 25, no. 4, pp. 464–475, 2006.
- [51] H. Zheng, Y. Qin, Y. Gu, F. Xie, J. Yang, J. Sun, and G.-Z. Yang, "Alleviating class-wise gradient imbalance for pulmonary airway segmentation," *IEEE Trans. on Med. Imaging*, vol. 40, no. 9, pp. 2452–2462, 2021.
- [52] G. Jin, C. Liu, and X. Chen, "An efficient deep neural network framework for COVID-19 lung infection segmentation," *Inf. Sci.*, vol. 612, pp. 745–758, 2022.
- [53] N. Saeezadeh, S. Minaee, R. Kafieh, S. Yazdani, and M. Sonka, "Covid tv-unet: Segmenting COVID-19 chest CT images using connectivity imposed unet," *Comput. methods programs biomedicine update*, vol. 1, p. 100007, 2021.
- [54] L. Fan, S. Liu, Q. Li, H. Yu, and X. Xiao, "Multidetector CT features of pulmonary focal ground-glass opacity: differences between benign and malignant," *The Br. journal radiology*, vol. 85, no. 1015, pp. 897–904, 2012.
- [55] S. Ruder, "An overview of multi-task learning in deep neural networks," *arXiv preprint arXiv:1706.05098*, 2017.